Theor Chim Acta (1991) 78: 365–395

Theoretica Chimica Acta

The ring opening of cyclopropylidene to allene: key features of the accurate reaction surface

S. Xantheas*, S. T. Elbert, and K. Ruedenberg

Ames Laboratory-USDOE** and Department of Chemistry Iowa State University, Ames, IA 50011, USA

Received August, 1990/Accepted September 5, 1990

Summary. The global potential energy surface, determined in the first paper [1] for the groundstate ring opening of cyclopropylidene to allene, is complemented by accurate calculations of its key regions. The basis set is extended and polarization functions are included. The full configuration space of four electrons in four reactive orbitals is enlarged to the full configuration space of eight electrons in eight active orbitals by including correlations in the unbroken, but stretched CC sigma bonds. The effect of further single and double excitations is examined. The geometries and relative energies of the critical regions are found to change only little except for the ring-opening energy barrier which is lowered to about 7 kcal/mol, in good agreement with the experimental estimate of about 6 kcal/mol. Furthermore, the bifurcation is shown to occur *after* the transition state, in the neighborhood of a conical intersection on the steepest descent path from the ring-opening transition state to the allene isomerization transition state. The steepest descent paths and the conical intersection are documented in detail. The cogwheel-like free internal rotation of the two methyl groups is confirmed by the accurate calculations. A similar richness of features is believed to exist on many potential energy surfaces governing chemical reactions.

Key words: Cyclopropylidene to allene – Potential energy surface – Extended basis sets – Enlarged configuration spaces

1. Introduction

The first paper of this series [1] (hereafter referred to as paper I) furnished a global overview over the potential energy surface governing the ring opening of cyclopropylidene to allene in terms of three internal coordinates, namely the ring-opening angle Φ and two dihedral angles δ_1 and δ_2 which describe the rotations of the two CH_2 groups with respect to the CCC plane. (The geometry and the coordinates are displayed in Figs. 1 and 2 of paper I.) The remaining 12

** *Present address:* Molecular Sciences Research Center, Pacific Northwest Laboratory, Richland, WA, 99352, USA

** Operated for the U.S. Department of Energy by Iowa State University under Contract No. 7405-Eng-82. This work was supported by the Office of Basic Energy Sciences

internal coordinates were relaxed by energy minimization for every $(\phi, \delta_1, \delta_2)$ triple. Limitations in computational power dictated the use of a minimal basis set and a small full configuration space to accomplish this overview.

While STO-3G based are known to yield reasonable geometries in general, and in particular in the case of hydrocarbons [2], it is also known that extended basis sets better describe strong π-bonds, such as occur in allene, and that polarization functions will lead to stronger bent bonds in rings, such as occur in cyclopropylidene. Moreover, the lack of flexibility in the minimal basis set tends to overestimate activation energies. Less serious is presumably the other limitation, namely the choice of the full space of 20 configurations generated by four electrons distributed over four "reactive" orbitals (two on the central carbon and one on each end carbon) between which electrons are rearranged to break bonds and form different bonds [3].

In the present paper we establish the connection between the global surface of paper I and the accurate potential energy surface by redetermining the key regions using extended basis sets and enlarged configuration spaces. These calculations yield reliable quantitative values for the reaction path and the critical energy differences. In particular, we examine the reactant cyclopropylidene, the product allene, the region around the ring-opening transition state, the ring-opening reaction path, the allene isomerization reaction path, and also the isoenergetic shelf corresponding to the cogwheel-like synchronized rotation found for the two CH_2 groups. The results indicate that the calculations of paper I provide a correct picture of the global potential energy surface, that the topography around the transition state requires a significant qualitative correction, and that the quantitative value of the ring-opening barrier is considerably lowered. A new feature found is that the bifurcation occurs *after* the transition state, close to a conical intersection on the steepest descent path.

2. Method of calculation

2.1. Scope of calculations

The number of energy calculations required for the reproduction of the entire reduced energy surface is of the order of 25 panels × 50 points/panel × 10 searches/point × 10 iterations/search = 125,000 MCSCF iterations, where we have used average values of 10 searches/point on the reduced energy surface to optimize the remaining 12 internal coordinates, and 10 iterations to converge each MCSCF energy calculation. A panel is a 2-dimensional cut through the 3-dimensional reduced energy surface where the energy is expressed as a function of the two dihedral angles δ_1 and δ_2 for a constant value of Φ. Additional CPU time is required for the evaluation of the gradient of the energy with respect to the nuclear coordinates in order to optimize the 12 remaining internal coordinates for each $(\phi, \delta_1, \delta_2)$ triple. The number of gradient evaluations is 25 panels × 50 points/panel × 10 searches/point × 1 grad./search = 12,500 gradient evaluations. Table 1 lists the estimated CPU times needed to carry out these calculations for the STO-3G basis and *for an extended basis* within the original FORS space (20 configurations) using the GAMESS program on various computers. Since the calculation of the entire surface for the extended basis was unrealistic when this research was done, only the aforementioned key regions were investigated by the more accurate procedures.

Table 1. CPU time needed to compute the entire reduced energy surface[a]

Machine	STO-3G basis	Dunning–Hay[b] basis
VAX-11/780	0.60	40.00
FPS-164	0.12	6.13
SCS-40		1.25
CRAY-1/XMP		0.43

[a] In CPU years using the GAMESS program
[b] Projected time

2.2. Basis sets

The following basis sets were used to improve the quality of calculations beyond that of the STO-3G basis (basis i):

Basis (ii): A Dunning–Hay basis set plus polarization functions on carbon consisting of the segmented contractions $(9s5p1d/3s2p1d)$ for carbon and $(4s/2s)$ for hydrogen. For the polarization function on carbon the exponent $\zeta_C = 0.75$ was chosen [4].

Basis (iii): The basis set of (ii) plus p-type polarization functions on hydrogen with exponent $\zeta_H = 1.0$ [5].

Basis (iv): A very large even-tempered Gaussian basis [6] of double-zeta quality contracted by the scheme [7] $(14s7p1d/3s2d1p)$ for carbon and $(6s/2s)$ and hydrogen, with the hydrogen exponents scaled by 1.2. The d polarization function exponents were the same as those for basis (ii).

These basis sets contain 106, 118, and 147 primitive atomic orbitals, contracted to 53, 65, and 53 quantitative basis orbitals, respectively.

The geometry optimizations of the reactant, transition state, product, and the allene isomerization transition state were performed with basis sets (ii) and (iii) using the GAMESS [8] program. The calculations with the large even-tempered Gaussian basis (iv) set were performed using the ALIS [9] program.

2.3. Configuration spaces

The original full configuration space of four electrons in four reactive orbitals (two on the central carbon and one on each end carbon), consisting of 20 configurations and hereafter referred to as FORS1, was used to optimize the geometries of the reactant, product, and transition states using the extended basis sets (ii) and (iii). In order to get an indication for additional correlations among these four electrons, CI calculations were performed for these optimized geometries in the space of the 13,700 configurations generated by taking all single and double excitations from the SCF wavefunction to the MCSCF reactive and virtual orbitals.

Next, the set of orbitals which generate the full active space was extended to include four additional molecular orbitals, namely a CC σ-bonding MO and a

CC σ-antibonding MO in each of the two CC bonds. The resulting FORS space, arising from distributing eight electrons over eight orbitals in all possible ways and hereafter referred to as FORS2, is spanned by 1764 configurations. (In the previous 20-dimensional FORS1 space, the CC σ-bonding MOs had been doubly occupied core orbitals, whereas the CC σ-antibonding MOs had remained unoccupied.) This enlargement of the full configuration space is intended to account for correlation changes in the CC σ-bonds whose lengths do change during the ring opening, in contrast to the rather invariant CH bonds.

Starting orbitals for the two CC σ-bonding MOs were obtained by localizing the core orbitals of the previous 20-configuration FORS1 calculation, using the Edmiston–Ruedenberg procedure [10]. This localization separates the core MOs into three carbon 1*s* shells, four CH bonds and two CC bonds. Starting orbitals for the CC σ-antibonding MOs can be similarly obtained by localization of the virtual orbitals of the previous calculation which separates the CH antibonds from the CC antibonds. Since the regions investigated here have either C_s or C_{2v} symmetry, localization *within each symmetry species only* is sufficient to achieve the desired separations in space between CC bonds and CH bonds, and this was done for the core orbitals. Moreover, an inspection of the virtual orbitals revealed that two of these MOs had already the desired CC antibonding character approximately and they were chosen without further localization as MCSCF starting orbitals. After completion of the MCSCF optimizations in the enlarged FORS space, all optimized orbitals were examined and it was found that the new MOs had indeed the desired CC σ-bonding and antibonding character. Thus, the correlation improvement had not migrated into the CH bonds.

For all choices of the coordinate triples $(\phi, \delta_1, \delta_2)$ for which the 1764 configuration wavefunction was determined, the geometries of the twelve secondary internal coordinates were reoptimized using the bases set (ii) as had been done for the 20-dimensional FORS space.

Table 2 gives a summary of the theoretical and computational methods used and how they will be referred to in the sequel. For example, (FORS1/ii) means a 20-configuration calculation with basis set (ii).

Table 2. Theoretical and computational methods

Method	Internal coordinates		Calculational procedure		
	Φ, δ_1, δ_2	Other 12	AO basis	No. of configurations	Optimization
FORS1/i	Entire surface	Optimized	MBS(STO-3G)	20	MC-SCF
FORS1/ii	Critical points	Optimized	DH + d on C	20	MC-SCF
	Reaction paths	Calculated	DH + d on C	20	MC-SCF
FORS1/iii	Critical points	Optimized	DH + d on C/p on H	20	MC-SCF
FORS1/iv	Critical points	From line 2	Even tempered	20	MC-SCF
CI/ii	Critical points	From line 2	DH + d on C	13700	CI
FORS2/ii	Critical points	From line 2	DH + d on C	1764	MC-SCF

3. Critical regions

3.1. The ring opening transition state

The region around the ring-opening transition state is the main place among the key regions on the potential energy surface where the results of the more accurate calculations differ from those of the first paper [1] in more than quantitative detail. We therefore begin by discussing this region.

In the previous calculation [1] (FORS1/i) the reaction path bifurcated, breaking C_s symmetry, *before* the transition state. There were thus two transition states, both of C_1 symmetry and being each other's mirror images with respect to the C_s mirror plane perpendicular to the CCC plane. However, as discussed in Sect. 6 of the first paper [1], the deviation of these transition states from C_s symmetry was only small and, more importantly, the energy changed only little on a path leading from one of these transition states to the other, the maximum occurring at the midpoint which has C_s symmetry, i.e., at the C_s-average of the two transition states. The energy of this "average transition state" lies only 0.2 kcal/mol above that of the two transition states having C_1 symmetry. While the reliability of such a detailed prediction by a STO-3G-based calculation was clearly open to question, it seemed likely that the actual energy surface would indeed be quite flat in this entire region.

In view of this feature, it was furthermore likely that the transition state would shift in a more accurate calculation and the first question of interest was therefore to establish the location of the transition state obtained by such a calculation. Thus, using the extended basis (ii) and the original 20-dimensional FORS1 space, a transition state search was initiated at one of the transition states found in the first paper [1]. This search led to a moderate displacement of this transition state. While the ring-opening angle Φ was virtually unchanged, the two CH_2 rotation angles δ_1 and δ_2 were changed by about 6°. All internal coordinates are listed in row 6 of Table 3. These relatively minor changes in δ_1, δ_2 were, however, sufficient to yield a *transition state which has C_s symmetry.*

In order to confirm this result, we determined, at this level of theory, a part of the potential energy surface in the transition state region, comparable to the calculations reported in Sect. 6 of paper I. Figure 1 displays the results of this calculation in a manner similar to Fig. 17 of paper I. Energy contours are depicted in terms of the coordinates $\delta_+ = [(\delta_1 + \delta_2)/2 - 90°]$, $\delta_- = (\delta_1 - \delta_2)/2$, for a constant value of Φ. Three panels are given corresponding to $\Phi = 82°$, 84.45°, 87°. The contours are drawn in increments of 0.5 mhartree. Each panel is based on 21 calculated energy values. For each of these, the remaining 12 internal coordinates are optimized as mentioned before. It is seen that, *for each panel, the minimum lies on the axis $\delta_+ = 0$ which corresponds to geometries which have C_s symmetry.* Furthermore, the values of this *minimum energy for constant* Φ, considered as a function of Φ, has a maximum for $\Phi = 84.45°$. This point is therefore indeed a transition state. Diagonalization of the Hessian matrix at this point confirms this conclusion by yielding 14 positive eignevalues and one negative eigenvalue describing a C_s-preserving displacement corresponding to the reaction coordinate.

The simplest interpretation of these results is that, for the potential energy surface obtained by this type of calculation, the reaction path does not bifurcate before the transition state. Rather a C_s-preserving channel leads from the reactant up to and across the transition state and the reaction path bifurcates

Table 3. Optimized geometries of the critical points of the ground state reaction surface

	Φ	δ_1	δ_2	r_{01}	r_{02}	r_{11}	$r_{11'}$	r_{22}	$r_{22'}$	α_{011}	$\alpha_{011'}$	α_{022}	$\alpha_{022'}$	β_1	β_2
R	59.45	90.0	90.0	1.532	1.532	1.081	1.081	1.081	1.081	117.1	117.1	117.1	117.1	33.1	33.1
	60.00	90.0	90.0	1.504	1.504	1.078	1.078	1.078	1.078	116.1	116.1	116.1	116.1	35.8	35.8
	60.41	90.0	90.0	1.503	1.503	1.077	1.077	1.077	1.077	116.1	116.1	116.1	116.1	35.6	35.6
	58.62	90.0	90.0	1.549	1.549	1.077	1.077	1.077	1.077	115.7	115.7	115.7	115.7	36.4	36.4
TS	84.24	57.1	134.8	1.448	1.448	1.086	1.081	1.086	1.081	118.3	125.9	118.3	125.9	5.9	4.0
	84.45	51.0	129.0	1.422	1.422	1.079	1.077	1.079	1.077	117.8	127.2	117.8	127.2	1.3	1.3
	86.52	48.4	131.6	1.429	1.429	1.080	1.078	1.080	1.078	118.1	126.6	118.1	126.6	0.4	0.4
	82.37	51.3	128.7	1.449	1.119	1.079	1.078	1.079	1.078	116.7	128.1	116.7	128.1	0.3	0.3
P	180.0	0.0	90.0	1.320	1.320	1.083	1.083	1.083	1.083	121.5	121.5	121.5	0.0	0.0	
	180.0	0.0	90.0	1.324	1.324	1.076	1.076	1.076	1.076	120.9	120.9	120.9	120.9	0.0	0.0
	180.0	0.0	90.0	1.323	1.323	1.076	1.076	1.076	1.076	120.9	120.9	120.9	120.9	0.0	0.0
	180.0	0.0	90.0	1.342	1.342	1.075	1.075	1.075	1.075	120.7	120.7	120.7	120.7	0.0	0.0
TS*	134.3	0.0	0.0	1.392	1.392	1.081	1.082	1.081	1.082	121.1	121.7	121.1	121.7	0.0	0.0
	135.0	0.0	0.0	1.385	1.385	1.076	1.076	1.076	1.076	121.0	121.0	121.0	121.0	0.0	0.0
	135.0	0.0	0.0	1.385	1.385	1.076	1.076	1.076	1.076	121.0	121.0	121.0	121.0	0.0	0.0
	135.0	0.0	0.0	1.385	1.385	1.074	1.077	1.074	1.077	121.0	120.8	121.0	120.8	0.0	0.0
	136.7	0.0	0.0	1.403	1.403	1.074	1.077	1.074	1.077	121.1	120.6	121.1	120.6	0.0	0.0

R: Cyclopropylidene; TS: transition state; P: allene; TS*: allene isomerization transition state
First entry: FORS1/i; second entry: FORS1/ii; third entry: FORS1/ii; fourth entry: FORS2/ii
Column labels: $r_{01} = C_0-C_1$ stretch; $r_{11} = C_1-H_1$ stretch; $r_{22} = C_2-H_2$ stretch
$r_{02} = C_0-C_2$ stretch; $r_{11'} = C_1-H_{1'}$ stretch; $r_{22'} = C_2-H_{2'}$ stretch
$\alpha_{011} = C_0-C_1-H_1$ bend; $\alpha_{022} = C_0-C_2-H_2$ bend; $\beta_1 = C_0-(C_1H_1H_{1'})$ out of plane bend
$\alpha_{011'} = C_0-C_1-H_{1'}$ bend; $\alpha_{022'} = C_0-C_2-H_{2'}$ bend; $\beta_2 = C_0-(C_2H_2H_{2'})$ out of plane bend
r in Å; α, β, δ, Φ in degrees

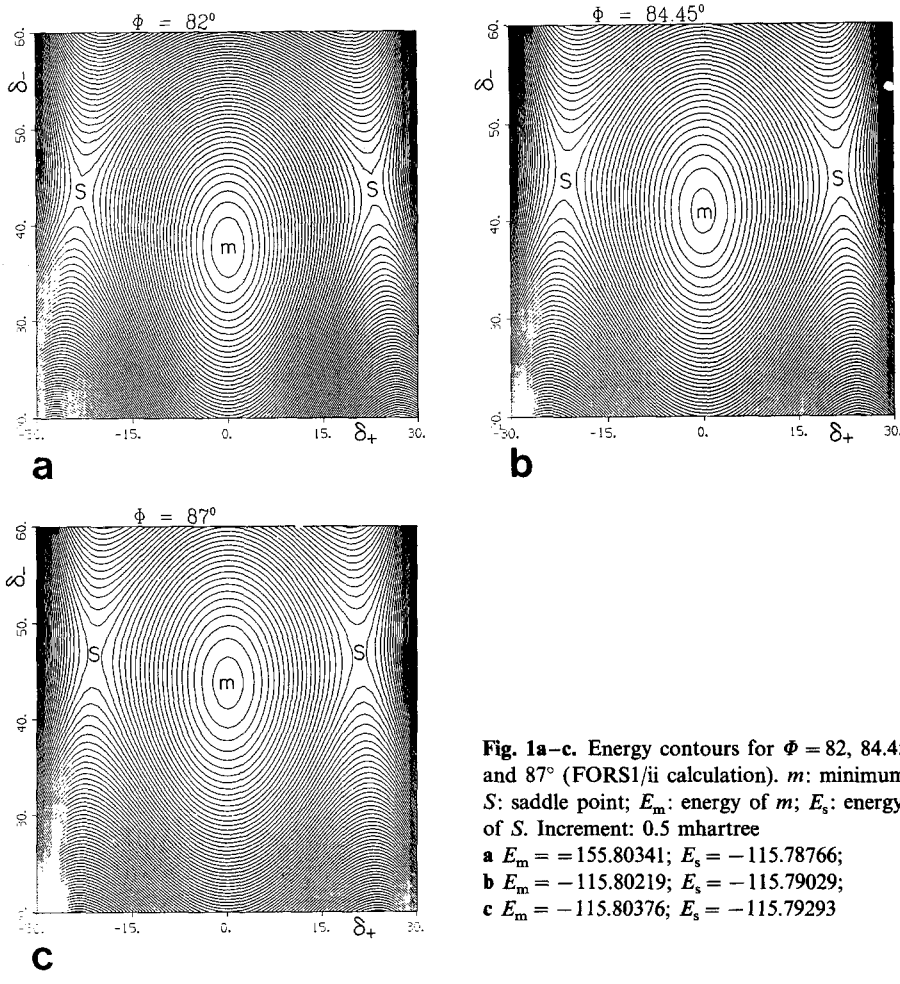

Fig. 1a–c. Energy contours for $\Phi = 82$, 84.45, and 87° (FORS1/ii calculation). *m*: minimum; *S*: saddle point; E_m: energy of *m*; E_s: energy of *S*. Increment: 0.5 mhartree
a $E_m = =155.80341$; $E_s = -115.78766$;
b $E_m = -115.80219$; $E_s = -115.79029$;
c $E_m = -115.80376$; $E_s = -115.79293$

thereafter. These conclusions were confirmed by calculating the steepest descent paths from the transition state to the reactant and towards the products. They will be displayed and discussed in Sect. 4.

In order to be sure that these conclusions remain valid for wavefunctions of higher accuracy, two further transition state searches were made, both starting with the transition state geometry just found. One search using the same FORS1 space but the basis set (iii), including hydrogen polarization functions, and another search using the basis set (ii) but the enlarged 1764 dimensional FORS2 space including CC σ-bond correlations. These calculations yielded only slightly displaced transition states, *both with* C_s *symmetry*. For the latter calculation the eigenvalue spectrum of the Hessian was redetermined and it turned out to be very similar to the one mentioned in the preceding paragraph.

The coordinates of these transition states are listed in rows 5 to 8 of Table 3. The two sets of normal mode frequencies are listed in Table 4a.

Finally, the influence of higher order correlations was examined through CI calculations in the configuration space spanned by all 13,700 single and double

Table 4a. Calculated normal mode frequencies (in cm^{-1})

	Cyclopropylidene	Transition state	Allene isomerization transition state
1	652.5	253.0i	1376.9i
	655.4	98.2i	1458.2i
2	883.4	702.3	357.6
	757.7	575.6	320.8
3	914.2	925.0	490.7
	865.5	971.6	473.0
4	920.9	982.0	664.9
	867.6	1027.9	725.3
5	1062.1	1038.2	669.0
	906.4	1043.0	734.4
6	1124.7	1053.8	987.1
	1072.6	1068.0	968.0
7	1136.4	1173.5	1054.4
	1100.9	1113.9	1005.0
8	1289.2	1312.5	1252.4
	1179.1	1170.3	1195.0
9	1368.8	1348.0	1419.5
	1375.2	1264.5	1373.3
10	1548.0	1606.0	1599.0
	1546.3	1601.7	1586.2
11	1585.4	1678.5	1616.7
	1572.9	1659.9	1601.0
12	3302.6	3306.5	3321.1
	3305.5	3299.1	3311.7
13	3306.2	3320.6	3333.4
	3310.7	3311.1	3319.1
14	3387.7	3395.9	3429.5
	3395.6	3392.8	3428.9
15	3403.6	3411.8	3445.8
	3409.5	3405.5	3444.1
Zero-point energy	37.0	36.1	33.8
	36.2	35.6	33.6

First entry: FORS1/ii calculation; second entry: FORS2/ii calculation
i denotes imaginary frequencies

excitations out of the four active orbitals of the dominant configuration of the 20-dimensional FORS1 space, using the orbital basis (ii). These calculations were performed for all points of the panel for $\Phi = 84.45°$ on Fig. 1, using the geometric parameters of the former calculations. The new calculations lead to the contour plot exhibited in Fig 2, which is almost quantitatively identical with

Table 4b. Comparison between experimental and calculated frequencies of the normal modes of allene

Frequency (cm^{-1})	Assignment	Experimental[a]		Calculated[b]	
		Raman	IR	FORS1	FORS2
$\nu_{11}(e)$	C=C=C bending	535		189.4	313.4
$\nu_4(b_1)$	C=C=C twisting	820		890.6	883.9
$\nu_{10}(e)$	C=C=C bending	838	852	790.7	870.2
$\nu_9(e)$	CH_2 rocking		1031	1055.5	1057.9
$\nu_3(a_1)$	C=C	1071		1125.5	1076.6
$\nu_7(b_2)$	CH_2		1389	1563.9	1597.3
$\nu_2(a_1)$	CH_2	1432		1618.0	1551.4
$\nu_6(b_2)$	C=C	1956	1980	2065.0	1954.3
$\nu_5(b_2)$	CH		2960	3339.5	3337.5
$\nu_1(a_1)$	CH	2993		3347.0	3341.6
$\nu_8(e)$	CH	3061		3432.4	3443.4
Zero-point E (kcal/mol)				35.6	35.9

[a] Herzberg (1966) p. 640
[b] With basis set (ii)

the corresponding plot of Fig. 1 (except, of course, for the absolute value of the energy at the minimum): For both plots, the minimum occurs at the same position, the energy difference between the saddle points and the minimum is about 10 kcal/mol and the increment is 0.5 mhartree.

Thus, all calculations involving the larger basis sets (ii) and (iii) lead to a transition state with C_s symmetry and we conclude that the transition state region of the *actual* energy surface is adequately depicted by the displayed contour plots. Consequently, the channel leading up to the ring-opening transition state as well as the channel leaving the transition state preserve C_s symmetry

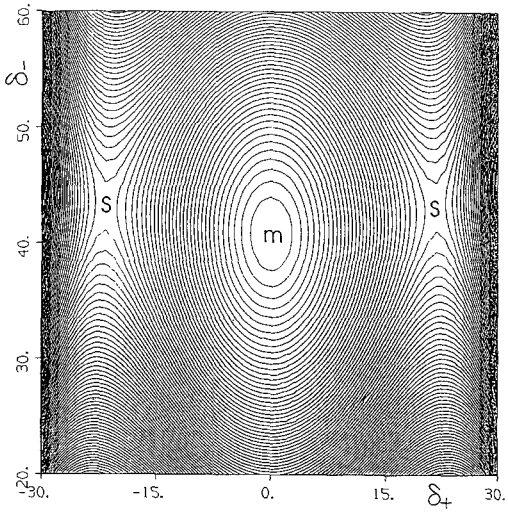

Fig. 2. Energy contours for $\Phi = 84.45°$ (singles and doubles CI calculation from the SCF configuration with basis set ii). Total of 13,700 configurations. *m*: minimum, *S*: saddle point. Increment: 0.5 mhartree

and the bifurcation of the reaction path into two branches, which are each other's mirror images and lead to the two isomeric products, must occur after the transition state. The basis set improvement from the STO-3G basis to the extended bases leads therefore to a shift of the bifurcation from *before* to *after* the transition state. A general discussion of the location of bifurcations with respect to a transition state and of the corresponding surface topographies has been given in a previous publication [11].

Because of the flatness of the energy surface in this region, this *qualitative* change is, however, the result of relatively small *quantitative* changes on the energy surface. The contour patterns of Fig. 1 and those of Fig. 17 in paper I are not dissimilar. In both cases, the pattern *for a given* Φ exhibits a minimum on the C_s-preserving axis $\delta_+ = 0$ and two saddle points off this axis. The small relative changes between the two calculations lead to a shift of the transition state from C_1 to C_s symmetry because the energy value at the minimum and that at the saddle points, *considered as functions of* Φ, differ as follows: In Fig. 17 of paper I, the maximum of the minima *on* the C_s-preserving $\delta_+ = 0$ axis is *higher* than the minimum of the saddle points *off* the $\delta_+ = 0$ axis. In Fig. 1 of the present paper, on the other hand, the maximum of the minima *on* the $\delta_+ = 0$ axis always remains *below* the minimum of the saddle points *off* the $\delta_+ = 0$ axis.

3.2. The other critical points

In the preceding section we saw that the more accurate calculations lead to a somewhat different topography around the ring-opening transition state than was obtained in the first paper. For the other critical points, viz. the reactant cyclopropylidene, the product allene and the allene isomerization transition state the changes are less dramatic. As was done for the ring-opening transition state, the geometries of all these critical points were reoptimized with respect to all fifteen coordinates for the following levels of approximation: (a) the 20-configuration FORS1 space with basis set (ii); (b) the 20-configuration FORS1 space with basis set (iii); (c) the 1764-configuration FORS2 space with basis set (ii).

Table 3 also lists the results for these critical points. It can be seen that, for all calculations, the CC bond lengths change by more than 10% during the ring opening, whereas the CH bond lengths change by less than 0.2%. It can also be seen that inclusion of the hydrogen polarization orbitals [basis set (iii)] produces only negligible changes in geometries and energetics. It seems therefore justified to consider correlations in the CC σ-bonds, but not in the CH bonds. Overall, the geometries furnished by the calculations of the first paper are not changed greatly by the more accurate calculations. In fact, for allene, the only species for which experimental data are available, the results from paper I are somewhat closer to the experimental values [12] (CC = 1.308 Å, CH = 1.087 Å, angle HCH = 118.2°). These results support the confidence in the calculations of paper I as furnishing a good *overall* picture of the *global* energy surface.

The energies at all critical points are listed in Table 5 for the various levels of theory. The table also contains the results of calculations with a very large even-tempered Gaussian basis set [basis (iv) of Sect. 2.2]. The first row contains the energies resulting from the calculations of the first paper. However, also for these (FORS1/i) calculations, the ring-opening transition state energy listed is that at the *average* C_s geometry between the two actual (FORS1/i) transition states (which have C_1 symmetry). As mentioned in Sect. 3.1, the energy difference

Table 5. Energies (in hartree) at critical points on the ground-state reaction surface

AO basis, configuration space	Cyclopropylidene C_{2v}	Transition state C_s	Allene D_{2d}	Allene isomerization T.S., C_{2v}
Geometries optimized with minimal basis set				
FORS1/i	−114.39557	−114.33331	−114.49936	−114.43350
FORS1/iv	−115.82693	−115.80462	−115.93060	−115.86369
Geometries optimized with extended basis sets				
FORS1/ii	−115.92073	−115.80016	−115.92827	−115.85970
FORS1/iv	−115.82775	−115.80505	−115.93094	−115.86376
FORS1/iii	−115.82900	−115.80821	−115.93663	−115.86798
FORS2/ii	−115.87169	−115.85885	−115.98780	−115.91222
CISD from SCF/ii	−115.84768	−115.83590	−115.95347	−115.88093
Number of configurations[a]				
FORS1	8/20	12/20	12/20	4/20
FORS2	508/1764	900/1764	492/1764	432/1764
CISD from SCF	3603/13700	6912/13700	3580/13700	3163/13700

[a] First entry: configurations in the applicable symmetry group; second entry: number of configurations in C_1

between the two geometries is only 0.2 kcal/mol. The reason for choosing the C_s average is that this geometry was also used for the calculations in the second row with basis set (iv) because, from the results discussed in the preceding section, it is clear that the geometry optimization with this basis set would yield a ring-opening transition state with C_s symmetry.

At the bottom of Table 5, the number of configurations for the various FORS spaces are listed. In each case, the first number denotes the number of configurations that are left in the relevant irreducible representation of the applicable symmetry group indicated in the heading. This is the number of configurations pertinent for the energy calculation at the critical point. The second number is the number of configurations in C_1 symmetry which are required for calculations at slightly displaced geometries which are needed for determining the Hessian matrix.

The vibrational frequencies in cm^{-1} obtained by diagonalizing the hessians for two types of calculations (FORS1 and FORS2 with basis set (ii); rows 3 and 6 of Table 5) are listed in Tables 4a,b. Also listed are the total zero-point energies (in kcal/mol), viz. $(\sum_k h\nu_k/2)$ where the sum goes over all 15 frequencies for cyclopropylidene and allene, but only over the 14 real frequencies ($k = 2$ to 15) for the two transition states. Experimental values are available for allene and they are also listed in Table 4b.

Of interest to chemists are the energy differences between the various critical points. They are listed in Table 6 for the various levels of theory reported in Table 5. For the two types of calculations for which the vibrational analysis was performed, the energy differences including the zero-point energy corrections are also given. It is apparent that the ring-opening exothermicity and the allene isomerization barrier are remarkably independent of the level of theory used. However, as expected, the ring-opening barrier is significantly reduced by going

Table 6. Critical energy differences (in kcal/mol) for the ground-state reaction surface

AO basis, configuration space	Ring-opening exothermicity	Ring-opening barrier	Allene isomerization barrier
Geometries optimized with minimal basis set			
FORS1/i	−65.1	39.1	41.3
FORS1/iv	−65.1	14.0	42.0
Geometries optimized with extended basis sets			
FORS1/ii	−67.5	12.9	43.0
including ZPE	−68.9	12.0	41.2
FORS1/iv	−64.8	14.2	42.2
FORS1/iii	−67.5	13.0	43.1
FORS2/ii	−72.9	8.1	47.4
including ZPE	−73.2	7.5	45.1
CISD from SCF	−66.4	7.4	45.5

to the more accurate wavefunctions. This is essentially due to the extension of the basis set as is evident from the second row which differs from the first *only* in the increase in the size of the basis set (the configuration space and the geometry being the same). It reduces the barrier from 39 kcal/mol to 14 kcal/mol. Enlargement of the configuration space to include CC σ-bond correlations (row 6) lowers the barrier to about 8 kcal/mol and inclusion of higher-order correlations to 7.4 kcal/mol. From row 3 and 6 it is seen that the zero-point energy corrections to the barrier is about −0.5 to −1 kcal/mol. Combining this result with the barrier given in row 7, one can estimate a value around 7 kcal/mol. This inference is in agreement with the estimate of 5–6 kcal/mol which has been estimated from experimental results of related reactions [13].

4. Reaction paths

4.1. The steepest descent: qualitatively

The possible relationships between transition states, bifurcations, and reaction paths, modeled as steepest descent curves on an energy surface, have been discussed in detail in a previous paper [11]. One of the observations made was that steepest descent curves descending from a transition state with C_s symmetry either start out perpendicular to the C_s plane or lie in the C_s plane, in which case they maintain C_s symmetry until they meet another point where the gradient vanishes or is multivalued.

The steepest descent curves which are relevant for the energy surface obtained by the more accurate (FORS1/ii) calculations are shown in Fig. 3 in a style similar to that of Fig. 5a paper I: Reaction paths are shown as curves in the δ_1, δ_2 plane with the appropriate values of Φ indicated in parentheses at various points. As discussed in paper I, the alternative coordinate $\delta_+ = (\delta_1 + \delta_2)/2 - 90°$ breaks C_s symmetry, whereas $\delta_- = (\delta_1 - \delta_2)/2$ preserves C_s symmetry when $\delta_+ = 0$. The heavy lines depict the steepest descent paths passing through the

transition states. On them, the point R ($\Phi = 60.3°$) indicates the reactant cyclopropylidene and the point P on the line $\delta_+ = 45°$ ($\Phi = 180°$) denotes the product allene. Actually, the entire line $\delta_+ = 45°$ ($\Phi = 180°$), represents allene, a displacement along this line corresponding to a rotation of allene around its molecular axis. The line $\delta_+ = -45°$ ($\Phi = 180°$) corresponds to the isomeric mirror image of allene indicated by P′. The point TS ($\Phi = 84.5°$) is the ring-opening transition state and the point TS* ($\Phi = 135°$) is the transition state for the isomerization between the two allene isomers. The steepest descent lines emanating from TS preserve C_s symmetry, one ending at the reactant R, the other at the transition state TS*. The downhill steepest descent lines starting at TS* and ending at the two isomeric allene products P and P′ do not preserve C_s symmetry.

Since TS* is a normal second-order saddle point and the downhill directions are towards the allenes, the steepest descent line arriving at TS* from TS must do so on a ridge and this is confirmed by the normal mode frequencies listed in Table 4a. However, at TS this steepest descent line starts out as a downhill valley, as can also be seen from the normal modes in Table 4a as well as from the discussion in Sect. 3.1, in connection with Fig. 1. Consequently, the steepest path from TS to TS* must turn from a valley into a ridge some place in between: i.e., it has a valley-ridge inflection point [11].

There exists, however, a further complication due to the fact, discussed in Sect. 4.3 of the preceding paper [14] (paper II), that the ground-state wavefunction at the transition state TS belongs to a different irreducible representation with respect to the C_s mirror plane than the ground-state wavefunction at the transition state TS*. At TS, the irreducible representation is A′, at TS* it is A″. It follows that, *in the C_s-preserving internal coordinate subspace*, there are two states, one of symmetry A′, the other of symmetry A″ such that $E(A'') > E(A')$ at TS and $E(A') > E(A'')$ at TS*. These two systems cross between TS and TS* at a point which is denoted by CR on Fig 3. *Outside the C_s subspace*, both states belong to the *same* irreducible representation, namely A of C_1.

We shall see that, *near* the intersection CR, the lower surface is a *ridge* on the A′ side as well as on the A″ side of CR. The steepest descent path starting out as a valley at TS must therefore turn into a ridge at a point before reaching CR.

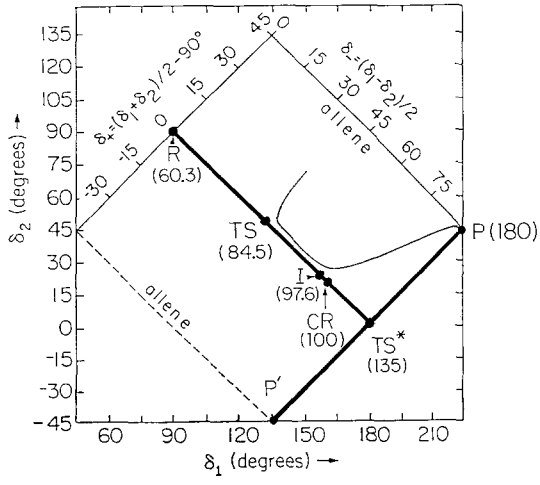

Fig. 3. Reactions paths (FORS1/ii calculation) in the (Φ, δ_1, δ_2) space. *Heavy line*: steepest descent lines through saddle points; *thin line*: steepest descent line starting *near* TS (for the sake of clarity, the mirror image of this line leading to P′ is not shown). *R*: Cyclopropylidene, *TS*: ring-opening transition state, *I*: valley-ridge inflection point, *CR*: intersection, *TS**: allene isomerization transition state, *P*, *P′*: allene. For all these points the Φ values are given in parentheses

This point on the A′ curve is denoted as I (for "inflection") on Fig. 3. The steepest descent path along the A″ curve from CR to TS*, on the other hand, remains a ridge all the way. The steepest descent paths from TS* to the two allene products P, P′ are valleys.

Finally, it will be seen that, at the crossing point CR, the gradient continues to point in a C_s-preserving direction. Hence, following the steepest descent on A′ from TS to CR and on A″ from CR to TS*, the path will run at first along the floor of a valley, then atop a ridge. It is evident that dynamic trajectories will not stay atop the ridge, but fall off it due to slight random destabilizations. Therefore, if one wishes to use steepest descent lines as rough models for reaction paths which end up at the allene products, then the only option is to start anew at a reasonable point nearby I or CR on a different, C_s symmetry-breaking steepest descent path. Such a restart is also justified in view of the bifurcating character of the steepest descent lines *near* the ridge, which will be discussed on Sect. 5.4. Whether the neighborhood of the valley-ridge inflection point I or that of the crossing point CR is most appropriate for this restart, is of no consequence in this case since the two points lie so close to each other. The steepest descent along a C_s symmetry breaking path is shown as a light line on Fig. 3.

We shall now substantiate and elaborate upon this qualitative description in quantitative detail. The following discussion is based on calculations made at the (FORS1/ii) level.

4.2. The steepest descent: quantitatively

From R to TS. First, as mentined in Sect. 3.1, the steepest descent curve from the ring-opening transition state TS to the reactant R (cyclopropylidene) was determined. It preserves C_s symmetry and corresponds to the straight line between C and TS in Fig. 3. The values of the ring-opening angle Φ are given in parentheses. The energy along this path is displayed as a function of Φ in Fig. 4 by the curve between R and TS. It is denoted by ^{1}A′, the irreducible representation of this state in C_s. Figure 4a exhibits the quantitive plot of E versus Φ. Figure 4b is a schematic perspective drawing of E versus the symmetry-preserving coordinate Φ and the symmetry-breaking coordinate δ_+. The dependence upon the symmetry-preserving coordinate δ_- and the secondary coordinates γ_j is suppressed.

Table 7 lists the energy and all 15 coordinates for a number of points on the steepest descent path.

From TS to CR. Next, the steepest descent path from the transition state TS towards increasing values of Φ was determined. In principle, this path preserves C_s symmetry. However, because numerical problems can be expected after $\Phi = \Phi(\mathrm{I})$, when the path runs atop a ridge, the steepest descent calculations were performed under restriction to C_s symmetry with the wavefunction restricted to the A′ irreducible representation. The energy is displayed as a function of Φ by the remainder of the curve denoted by ^{1}A′ in Fig. 4. It is seen to descend *very* slowly to a minimum at a ring-opening angle of about $\Phi = 106.5°$ which lies only 2 kcal/mol lower than the transition state TS.

We then determined the energy of the lowest A″ state along the same path in internal coordinate space, i.e., *all internal coordinates were chosen to be identical to those of the steepest descent path of the A′ state listed in Table 7.* This energy

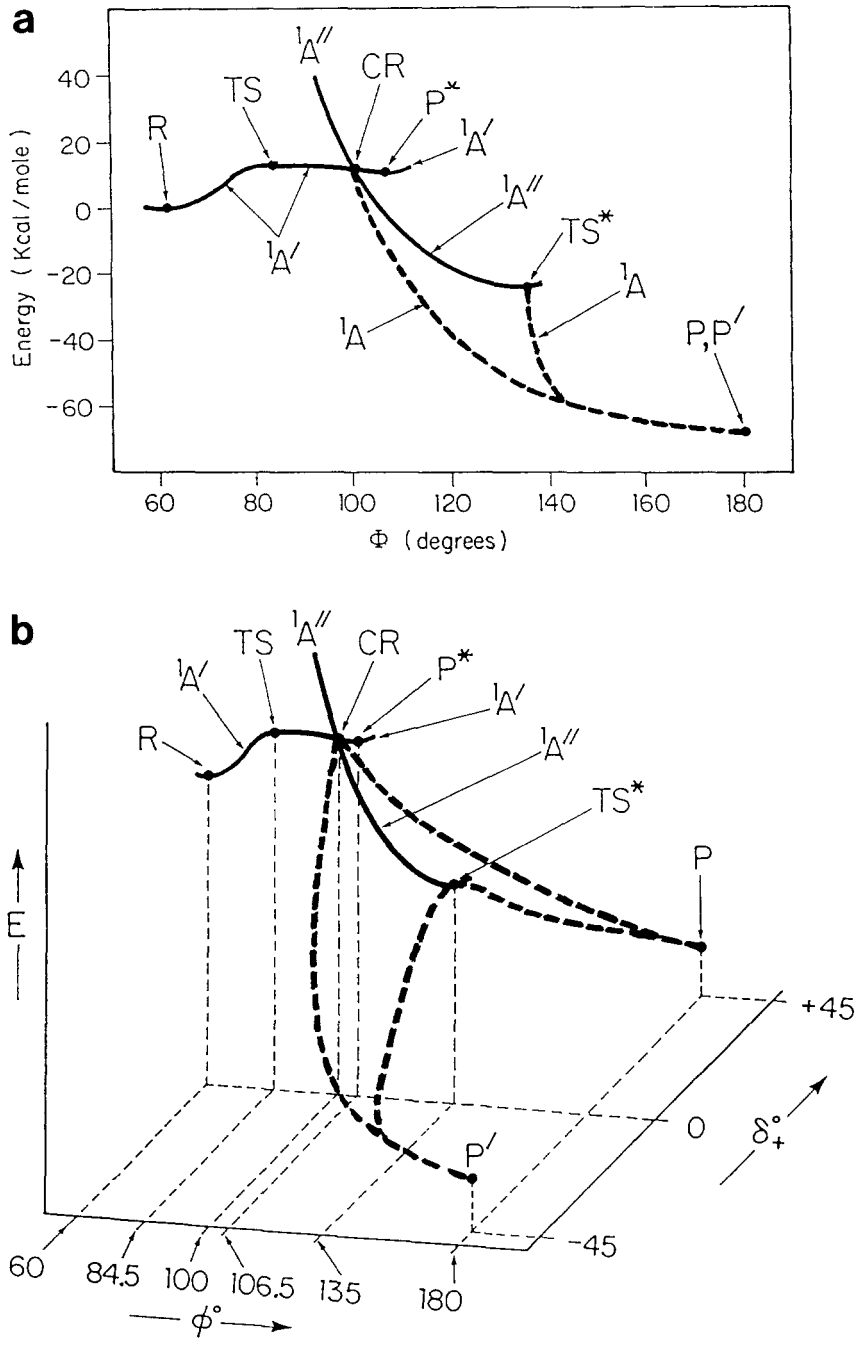

Fig. 4a,b. Variation of the energy along the various reaction paths (FORS1/ii calculation). **a** Quantitative plot of E versus Φ from values in Table 8. **b** Semiquantitative perspective plot of E versus Φ and δ_+. *Bold solid lines*: C_s-preserving paths; *bold dashed lines*: C_s-breaking paths. The meaning of the various points on the paths is the same as in Fig. 3. P* is the minimum on the $^1A_1$ excited state surface

Table 7. Internal coordinates of points along the various reaction paths (FORS1/ii calculations)

	Φ	δ_1	δ_2	r_{01}	r_{02}	r_{11}	$r_{11'}$	r_{22}	$r_{22'}$	α_{011}	$\alpha_{011'}$	α_{022}	$\alpha_{022'}$	β_1	β_2	Energy
From R (cyclopropylidene) to P* (^{1}A′ planar allene) via TS on the ^{1}A′ surface																
R	60.33	90.0	90.0	1.532	1.532	1.081	1.081	1.081	1.081	117.1	117.1	117.1	117.1	33.1	33.1	−115.82073
	60.76	87.2	92.8	1.501	1.501	1.083	1.079	1.083	1.079	116.3	117.1	116.3	117.1	33.6	33.6	−115.82002
	61.66	84.2	95.8	1.495	1.495	1.086	1.077	1.086	1.077	116.1	117.1	116.1	117.1	34.4	34.4	−115.81923
	63.30	80.2	99.8	1.487	1.487	1.080	1.079	1.080	1.079	116.0	118.8	116.0	118.8	31.9	31.9	−115.81749
	66.44	74.1	105.9	1.472	1.472	1.081	1.078	1.081	1.078	116.0	121.7	116.0	121.7	26.6	26.6	−115.81232
	69.34	69.4	110.6	1.460	1.460	1.083	1.078	1.083	1.078	116.2	123.8	116.2	123.8	21.5	21.5	−115.80776
	72.07	65.5	114.5	1.449	1.449	1.085	1.077	1.085	1.077	116.5	125.3	116.5	125.3	16.8	16.8	−115.80446
	78.00	60.00	120.0	1.422	1.422	1.079	1.079	1.077	116.3	116.3	128.5	116.3	128.3	4.2	4.2	−115.89045
TS	84.45	51.0	129.0	1.422	1.422	1.079	1.077	1.079	1.077	117.8	127.2	117.8	127.2	1.3	1.3	−115.80016
	92.41	41.4	138.6	1.415	1.415	1.091	1.078	1.091	1.078	118.9	126.2	118.9	126.2	3.2	3.2	−115.80042
	94.00	39.1	140.9	1.414	1.414	1.093	1.078	1.093	1.078	119.1	126.0	119.1	126.0	3.6	3.6	−115.80058
	95.52	36.7	143.3	1.414	1.414	1.094	1.077	1.094	1.077	119.4	125.7	119.4	125.7	3.9	3.9	−115.80077
	97.01	34.2	145.8	1.413	1.413	1.095	1.077	1.095	1.077	119.7	125.5	119.7	125.5	4.0	4.0	−115.80098
	98.53	31.4	148.7	1.413	1.413	1.096	1.076	1.096	1.076	119.9	125.3	119.9	125.3	4.0	4.0	−115.80124
CR	100.33	27.6	152.4	1.412	1.412	1.097	1.075	1.097	1.075	120.2	125.0	120.2	125.0	3.8	3.8	−115.80157
	101.00	21.8	158.2	1.416	1.416	1.084	1.080	1.084	1.080	120.4	125.0	120.4	125.0	2.9	2.9	−115.80211
	104.50	1.7	178.3	1.417	1.417	1.085	1.080	1.085	1.080	121.1	124.6	121.1	124.6	0.2	0.2	−115.80305
P*	106.48	0.0	180.0	1.414	1.414	1.086	1.080	1.086	1.080	120.9	124.5	120.9	124.5	0.0	0.0	−115.80328
From TS to TS* (allene isomerization transtion state) on the ^{1}A″ surface																
	92.41	41.4	138.6	1.415	1.415	1.091	1.078	1.091	1.078	118.9	126.2	118.9	126.2	3.2	3.2	−115.75900
	96.53	35.0	145.0	1.413	1.413	1.095	1.077	1.095	1.077	119.6	125.6	119.6	125.6	4.0	4.0	−115.78232
	98.53	31.4	148.7	1.413	1.413	1.096	1.076	1.096	1.076	119.9	125.3	119.9	125.3	4.0	4.0	−115.79273
CR	100.33	27.6	152.4	1.412	1.412	1.097	1.075	1.097	1.075	120.2	125.0	120.2	125.0	3.8	3.8	−115.81057
	101.94	27.1	152.9	1.407	1.407	1.082	1.074	1.082	1.074	121.2	123.3	121.2	123.3	3.9	3.9	−115.80867
	105.44	25.7	154.3	1.396	1.396	1.075	1.072	1.075	1.072	120.3	123.1	120.3	123.1	3.9	3.9	−115.81999

	110.46	22.8	157.2	1.388	1.388	1.075	1.071	1.075	1.071	117.5	125.1	117.5	125.1	3.8	3.8	−115.83259
	116.13	17.9	162.1	1.385	1.385	1.078	1.068	1.078	1.068	116.6	125.6	116.6	125.6	3.0	3.0	−115.84416
	122.08	11.1	168.9	1.384	1.384	1.079	1.073	1.079	1.073	117.4	124.7	117.4	124.7	1.8	1.8	−115.85323
	127.91	4.5	165.5	1.384	1.384	1.078	1.072	1.078	1.072	118.8	123.2	118.8	123.2	0.7	0.7	−115.85791
	133.42	1.0	179.0	1.385	1.385	1.077	1.075	1.077	1.075	120.6	121.8	120.6	121.8	0.1	0.1	−115.85946
TS*	135.00	0.0	180.0	1.385	1.385	1.076	1.076	1.076	1.076	121.0	121.0	121.0	121.0	0.0	0.0	−115.85970
From TS* (allene isomerization transition state) to P(D_{2d} allene) via a C_1 route																
TS*	135.0	0.0	180.0	1.385	1.385	1.076	1.076	1.076	1.076	121.0	121.0	121.0	121.0	0.0	0.0	−115.85970
	135.1	−5.3	174.7	1.384	1.384	1.974	1.075	1.073	1.075	121.1	121.0	121.2	120.9	1.4	1.4	−115.86316
	135.4	−11.7	168.4	1.380	1.380	1.380	1.380	1.071	1.059	1.067	1.063	121.4	120.8	2.9	2.9	−115.87282
	138.5	−27.9	152.1	1.356	1.356	1.071	1.116	1.084	1.105	123.1	119.5	123.0	119.6	6.0	6.0	−115.90119
	141.8	−36.1	144.1	1.342	1.342	1.056	1.121	1.079	1.105	123.8	118.6	123.6	118.7	6.6	6.6	−115.91119
	145.0	−40.2	140.1	1.337	1.337	1.044	1.118	1.071	1.101	123.9	118.2	123.7	118.4	6.6	6.6	−115.91534
	151.3	−43.5	136.8	1.332	1.332	1.039	1.110	1.060	1.094	123.5	118.4	123.4	118.5	5.9	5.9	−115.91982
	157.3	−44.2	135.6	1.328	1.328	1.050	1.114	1.059	1.110	122.4	119.0	122.4	119.5	4.9	4.9	−115.92268
	161.6	−44.6	135.6	1.327	1.327	1.050	1.111	1.055	1.103	122.0	120.0	122.0	119.9	4.2	4.2	−115.92396
P	180.0	−45.0	135.0	1.324	1.324	1.076	1.076	1.076	1.076	120.9	120.9	120.9	120.9	0.0	0.0	−115.92827
From CR (intersection point) to P(D_{2d} allene) via a C_1 route																
CR	100.3	27.6	152.4	1.412	1.412	1.097	1.075	1.097	1.075	120.2	125.0	120.2	125.0	3.8	3.8	−115.80157
	103.6	33.0	164.6	1.406	1.391	1.080	1.078	1.080	1.077	121.3	123.3	121.8	122.9	3.8	3.8	−115.82687
	111.8	40.2	173.2	1.377	1.373	1.072	1.049	1.075	1.046	126.3	117.6	123.9	119.5	6.8	−1.6	−115.85849
	117.0	45.0	−168.4	1.359	1.366	1.074	1.121	1.091	1.079	126.3	117.5	124.2	119.1	6.9	−3.7	−115.87502
	120.8	47.9	−163.6	1.351	1.360	1.066	1.123	1.094	1.075	126.1	118.9	124.1	118.9	6.8	−5.0	−115.88461
	130.5	52.7	−155.1	1.342	1.349	1.088	1.104	1.058	1.039	126.1	116.6	124.1	118.4	6.5	−7.0	−115.90145
	139.2	54.7	−150.6	1.334	1.340	1.096	1.116	1.063	1.049	124.8	117.5	123.4	118.7	6.0	−7.6	−115.91093
P	180.0	55.0	−145.0	1.324	1.324	1.076	1.076	1.076	1.076	120.9	120.9	120.9	120.9	0.0	0.0	−115.92827

is displayed, as a function of Φ by the left part of the curve labelled $^1A''$ in Fig. 4. It starts out higher than the A′ energy, decreases very rapidly and crosses the A′ curve at $\Phi = 100°$, which is thus the point CR.

In Fig. 3, the Φ values, given in parentheses along the straight line depicting the steepest descent path force TS to CR, are those of the A′ state.

Finally, we calculated energies at various points close to those on the steepest descent curve from TS to CR by choosing $\delta_+ = 0.5°$ instead of $\delta_+ = 0°$ and leaving all other 14 coordinates unchanged. We found that, for $\Phi = \Phi(\mathrm{I}) = 97.6°$, the energy *increase* with δ_+ changes into an energy *decrease* with δ_+. This point was therefore the valley-ridge inflection point I.

*From CR to TS**. For Φ larger than $\Phi(\mathrm{CR}) = 100°$, the curve $^1A''$ lies below the curve $^1A'$ in Fig. 4 and, hence, the ground state belongs to the irreducible representation A″ on this part of the C_s-preserving coordinate subspace. We therefore determined the ground-state steepest descent curve from CR to TS* under the restriction that the wavefunction belongs to A″ symmetry. Its energy is displayed as a function of Φ by the right part of the curve labelled $^1A''$ in Fig. 4. In Fig. 3, this steepest descent path is depicted by the straight line from CR to TS*, the Φ values in parentheses are those of the A″ state.

It is apparent that the A″ energies for $\Phi < 100$' and the A′ energies for $\Phi > 100°$ are part of the lowest excited state. It was verified that it has in fact a minimum, i.e., an equilibrium geometry at $\Phi = 106.5°$.

From TS to P and P′*. The steepest descent paths shown in Fig. 3 from TS* to the two allene products P, P′ are each other's mirror images. Again the appropriate Φ values are indicated in parentheses and the energy is displayed as a function of Φ in Fig. 4. This path is a model for the isomerization of the allene ground state.

From I/CR to P and P′. As discussed in Sect. 4.1, the C_s-preserving steepest descent path from I over CR to TS* is unsuited as a reaction path model because it runs atop a ridge. In contrast, the steepest descent lines *near* the ridge exhibit bifurcating behavior as will be seen in Sect. 5.4. Therefore, the region between I and CR is the region where the reaction path begins to bifurcate. We therefore determined a C_s-symmetry-breaking steepest descent curve which led directly to the product *P* by starting *near* the intersection point CR. All internal coordinates of this starting point were chosen as those of the point CR, except that $\delta_+ = 0°$ was replaced by $\delta_+ = 0.5°$. The resulting steepest descent curve is shown as a light line in Fig. 3 and its energy is displayed as a function of Φ in Fig. 4 by the curve denoted as ^1A. The mirror image of this steepest descent curve starts for $\delta_+ = -0.5°$ and leads to the mirror image product P′. It is shown in Fig. 4 but not in Fig. 3.

Figure 3 also shows a part of the light line for Φ values starting before CR (i.e., for Φ values less than 100°). We shall comment on this part in Sect. 5.4.

It should also be noted, however, that, at the intersection point, there exists a probability for a *diabatic* transition to the upper surface which would land the molecule in the minimum P* and initiate a different chemistry.

The internal coordinates and energies of the points on all of the various steepest descent paths are listed in Table 7.

5. The intersection coordinate subspace (ICS)

The point CR is not the only point where the two states E_1 and E_2 cross. In fact, there exists a multidimensional region in the coordinate space where $E_1 = E_2$. We call it the intersection coordinate subspace (ICS). In the present section we shall discuss this multidimensional potential energy surface intersection in some detail. We shall be particularly concerned with the *orthogonal trajectories* of the energy contours in the neighborhood of the point CR since the steepest descent curve from TS to CR is a model of the reaction path. We shall see that, near CR, the forces derived from the energy surface have a strong *bifurcating character*, a fact which justifies the restart off C_s symmetry discussed in the preceding section.

5.1. Dimensionality

Two potential energy surfaces do not have to intersect. However, if they do then it is to be expected (i.e., the opposite is highly unlikely) that there exist, embedded in the space spanned by all internal coordinates $q_1, q_2, \ldots, q_M$, *regions* having the character of multidimensional curvilinear linear surfaces on which $E_1 = E_2$. The ensemble of these regions forms the intersecting coordinate subspace for the two states. This ICS is determined by having to satisfy two conditions, namely [15]:

$$\Delta H(q_1, \ldots, q_M) = H_{11}(q_1, \ldots, q_M) - H_{22}(q_1, \ldots, q_M) = 0 \tag{5.1}$$

$$H_{12}(q_1, \ldots, q_M) = 0 \tag{5.2}$$

where H_{11}, H_{22}, H_{12} are hamiltonian matrix elements with respect to a certain many-electron function basis F_1, F_2. As indicated, they are functions of M internal coordinates $q_1, \ldots, q_M$ of the molecule. *In general, it is therefore to be expected* [15] *that, if Eqs.* (5.1, 2) *have any real solutions at all, then the solutions space, i.e., the ICS is a hyperspace of dimension* $(M - 2)$. This conclusion must be modified, however, in those cases where, for *all* values of the coordinates $q_1, \ldots, q_M$, the molecule is invariant under a symmetry group and the two intersecting states belong to different irreducible representations. In this situation the functional bases F_1, F_2 can be chosen as belonging to these two irreducible representations without reference to the hamiltonian of the system and, hence, the matrix element H_{12} vanishes identically for all values of $(q_1, \ldots, q_M)$. Consequently, F_1 and F_2 are in fact the two states and only Eq. (5.1) provides a true restriction. Thus, the ICS is of dimension $(M - 1)$ in this case. Similar reasoning applies if a coordinate *subspace* is invariant under some symmetry group, as will be seen below.

In the present case, the overall symmetry group is C_1 and the full internal coordiante species of dimension 15. Since C_1 has only one irreducible representation, the ICS is of dimension $15 - 2 = 13$.

There exists, however, as we have seen, a coordinate subspace in which the molecule has C_s symmetry. From Fig. 2 of paper I, it is apparent that the ring-opening coordinate Φ preserves C_s symmetry when it exists and that the remaining 14 internal coordinates $(\delta_1, \delta_2, \gamma_1, \gamma_2, \ldots, \gamma_{12})$ come in pairs such that, for each pair, the sum and the difference are either symmetric or antisymmetric with respect to the C_s symmetry plane. Let δ_+, γ_1', γ_2', $\ldots$, γ_6' denote the antisymmetric combinations and δ_-, γ_1'', γ_2'', $\ldots$, γ_6'' the symmetric ones. It follows then that the preservation of C_s symmetry is equivalent to the seven "C_s-symmetry-breaking" coordinates δ_+, γ_1', γ_2', $\ldots$, γ_6' remaining zero and, when this is the case, that the C_s-preserving coordinate subspace is spanned by the eight "C_s-symmetry-preserving" coordinates Φ, δ_-, γ_1'', γ_2'', $\ldots$, γ_6''.

Since, within this supspace, the two states under consideration belong to different irreducible representation of C_s (viz. A′ and A″), it follows from what has been said before that, within the C_s-preserving subspace, the ICS is of dimension $8-1=7$. Thus, of the 13 degrees of freedom the interesecting coordinate subspace has in C_1, seven maintain C_s symmetry and $13-7=6$ break C_s symmetry.

5.2. Linear approximation near CR

From Eqs. (5.1) and (5.2) it is apparent that, in the immediate neighborhood of CR, the ICS hypersurface coincides to first order with the *tangential hyperplane* which is perpendicular to the gradient of ΔH and that of H_{12} at CR. These two gradients have simple forms. First, since, as we have seen earlier, the energies vary quite slowly with the twelve secondary coordinate $\gamma_1, \gamma_2, \ldots, \gamma_{12}$, we can neglect the partial derivatives with respect to these coordinates. It is furthermore evident that H_{11} and H_{22}, and hence also ΔH, are *symmetric* with respect to deviations from C_s symmetry, whereas H_{12} is *antisymmetric* with respect to such displacements. Hence the partial derivative of ΔH with respect to the antisymmetric coordinate δ_+ vanishes as do the partial derivatives of H_{12} with respect to the symmetric coordinates Φ and δ_-. Expansion of the two conditions near CR in Eqs. (5.1) and (5.2) to first order yields therefore:

$$\Delta H = a_1\hat{\Phi} + a_2\hat{\delta}_- = a\xi = 0 \tag{5.3}$$

$$H_{12} = b\delta_+ = 0 \tag{5.4}$$

where

$$\begin{aligned} \hat{\Phi} &= \Phi - \Phi(\mathrm{CR}) = \text{displacement of } \Phi \text{ from CR} \\ \hat{\delta}_- &= \delta_- - \delta_-(\mathrm{CR}) = \text{displacement of } \delta_- \text{ from CR} \\ \delta_+ &= \delta_+ - \delta_+(\mathrm{CR}) = \text{displacement of } \delta_+ \text{ from CR} \end{aligned} \tag{5.5}$$

$$a_1 = [\partial(\Delta H)/\partial\Phi]_{\mathrm{CR}}, \quad a_2 = [\partial(\Delta H)/\partial\delta_-]_{\mathrm{CR}}, \quad b = [\partial H_{12}/\partial\delta_+]_{\mathrm{CR}} \tag{5.6}$$

and

$$\xi = (a_1\hat{\Phi} + a_2\hat{\delta}_-)/a, \quad \text{with } a = [a_1^2 + a_2^2]^{1/2} \tag{5.7}$$

It is now apparent that, near CR, the ICS is approximated by the 13-dimensional hyperplane defined by:

$$\delta_+ = 0, \qquad \xi = 0 \tag{5.8}$$

Consequently, the coordinates spanning the ICS hyperplane near CR are the six C_s-symmetry-breaking coordinates $\gamma_1', \gamma_2', \ldots, \gamma_6'$ as well as the seven C_s-symmetry-preserving coordinates $\gamma_1'', \gamma_2'', \ldots, \gamma_6''$ and

$$\eta = (a_2\hat{\Phi} - a_1\hat{\delta}_-)/a \tag{5.9}$$

The coordinates ξ, η are obtained from Φ, δ_- by an orthogonal transformation.

In fact, we shall see in the next section that $a_2 \ll a_1$, so that, approximately, $\xi \simeq \Phi$ and $\eta \simeq \delta_-$. The reason for this is as follows. The orbital analysis discussed in Sects. 4.2 and 4.3 of the preceding paper showed that the crossing of the A′ and the A″ energies is due to the shift of approximately one electron from the lone orbital on the central carbon, with A′ symmetry, to the nonbonding molecular orbital between the two end carbons, with A″ symmetry. This shift is a consequence of the fact that, as the ring opens, the orbital energy of the A′ orbital increases (due to increasing p character), whereas that of the A″ orbital

decreases (due to the increasing distance between the end atoms). Since these energy changes are essentially determined by the ring-opening angle Φ, one would indeed expect that, to first order, one has approximately:

$$\Delta H \simeq a_1 \hat{\Phi}, \tag{5.10}$$

Near CR, the ICS is then approximately the hyperplane satisfying:

$$\hat{\Phi} \simeq \Phi(\mathrm{CR}), \qquad \delta_+ \simeq \delta_+(\mathrm{CR}) = 0 \tag{5.11}$$

5.3. Determination of the linear approximation

Near the point CR on the ICS, the lower energy surface is given by the expression [15]:

$$E = E(\mathrm{CR}) + \bar{H} - [(\Delta H)^2 + (H_{12})^2]^{1/2} \tag{5.12}$$

where, in agreement with Eqs. (5.3)–(5.7), the terms ΔH and H_{12} are given by:

$$\Delta H = a_1 \hat{\Phi} + a_2 \hat{\delta}_- \tag{5.13}$$

$$H_{12} = b\delta_+ \tag{5.14}$$

and the term $\bar{H}$ is given by:

$$\bar{H} = (H_{11} + H_{22})/2 = c_1 \hat{\Phi} + c_2 \hat{\delta}_- \tag{5.15}$$

The partial derivative of $\bar{H}$ with respect to δ_+ vanishes for the same reason as it does for ΔH.

We determine d the coefficients a_1, a_2, b, c_1, c_2 as follows. After having found the crossing coordinates $\Phi(\mathrm{CR})$, $\delta_-(\mathrm{CR}$, and all $\gamma_j(\mathrm{CR})$, as described in Sect. 4.2, the energy of the molecule was calculated for the following geometries near CR:

(i)	$\hat{\phi} = 0$,	$\hat{\delta}_- = 0$,	$\delta_+ = 1°$	$\gamma_i = \gamma_i(\mathrm{CR})$ for all i
(iia)	$\hat{\phi} = 0$,	$\hat{\delta}_+ = 0$,	$\hat{\delta}_- = 1°$	$\gamma_i = \gamma_i(\mathrm{CR})$ for all i
(iib)	$\hat{\phi} = 0$,	$\hat{\delta}_+ = 0$,	$\hat{\delta}_- = -1°$	$\gamma_i = \gamma_i(\mathrm{CR})$ for all i
(iiia)	$\delta_+ = 0$,	$\hat{\delta}_- = 0$,	$\hat{\phi} = 1°$	$\gamma_i = \gamma_i(\mathrm{CR})$ for all i
(iiib)	$\delta_+ = 0$,	$\hat{\delta}_- = 0$,	$\hat{\phi} = -1°$	$\gamma_i = \gamma_i(\mathrm{CR})$ for all i
(iva)	$\delta_+ = 0$,	$\hat{\delta}_- = 1°$,	$\hat{\phi} = 1°$	$\gamma_i = \gamma_i(\mathrm{CR})$ for all i
(ivb)	$\delta_+ = 0$,	$\hat{\delta}_- = -1°$,	$\hat{\phi} = -1°$	$\gamma_i = \gamma_i(\mathrm{CR})$ for all i

Reference to Eqs. (5.11)–(5.15) shows that calculation (i) yields b, calculations (iia) and (iib) yield $|a_2|$ and c_2, calculations (iiia) and (iiib) yield $|a_1|$ and c_1, calculations (iva) and (ivb) yield $|a_1 + a_2|$ and $(c_1 + c_2)$. From calculation (ii), (iii), and (iv) one obtains a_1 and a_2 and one can check $(c_1 + c_2)$. The two sets of c_1 and c_2 agreed within 34.4 microhartree/degree, which confirmed the validity of the linear approximation. The following values were found:

$$\begin{aligned} a_1 &= 1729 \text{ microhartree} & a_2 &= 260 \text{ microhartree} \\ c_1 &= -1891 \text{ microhartree} & c_2 &= -325 \text{ microhartree} \\ b &= 93 \text{ microhartree.} \end{aligned} \tag{5.16}$$

5.4. Steepest descent lines near CR

Insertion of the values of Eq. (5.16) into the definition of Eqs. (5.7), (5.9) for ξ, η and into the energy expression of Eqs. (5.12) to (5.15) yields:

$$E - E(\mathrm{CR}) = -1918\xi - 40\eta - [(1748\xi)^2 + (93\delta_+)^2]^{1/2} \tag{5.17}$$

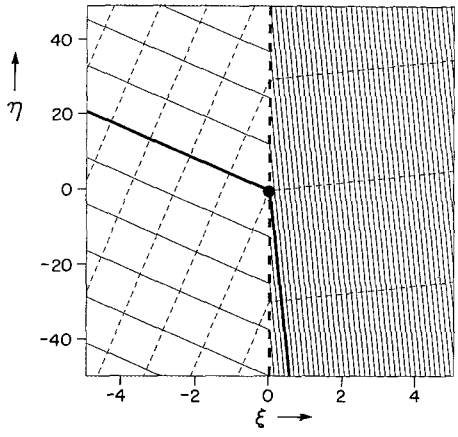

Fig. 5. Contours (*solid lines*) and orthogonal trajectories (*dashed lines*) of the surface $E - E(\mathrm{CR})$ for $\delta_+ = 0$ in the ξ–η plane (FORS1/ii calculation). The intersection point (CR) lies at the origin (*heavy dot*). *Heavy solid lines*: Contour $E - E(\mathrm{CR}) = 0$. Increment of contours: 0.5 mhartree. The *heavy dashed line* is the axis $\xi = 0$ (neither a contour nor an orthogonal trajectory)

where E is given in microhartrees and:

$$\begin{aligned} \xi &= 0.9889\hat{\phi} + 0.1487\hat{\delta}_- \\ \eta &= -0.1487\hat{\phi} + 0.9889\hat{\delta}_- \end{aligned} \tag{5.18}$$

Figure 5 exhibits contours of $E - E(\mathrm{CR})$ for $\delta_+ = 0$ in the plane of ξ and η, the C_s-preserving coordinates. The dashed line $\xi = 0$ is part of the ICS. On it the energy varies according to $E - E(\mathrm{CR}) = -40\eta$. (The other six coordinates of the ICS in C_s are $\gamma_1'', \gamma_2'', \ldots, \gamma_6''$.) The figure also displays the C_s-preserving steepest descent lines (it is apparent from Eq. (5.17) that $(\partial E/\partial\delta_+) = 0$ when $\delta_+ = 0$). The slow descent for $\xi < 0$ belongs to the A′ state, the steep descent for $\xi > 0$ belongs to the A″ state. In agreement with the statements at the end of Sect. 5.2, the steepest descent lines are nearly parallel to the ξ axis which, in turn, is very close to the $\hat{\Phi}$ axis.

Figure 6 exhibits, for $\eta = 0$, the energy dependence upon ξ and δ_+, the two coordinates responsible for the branching of the two energy surfaces, the former C_s-symmetry-preserving, the latter C_s-symmetry-breaking. In this figure, only the

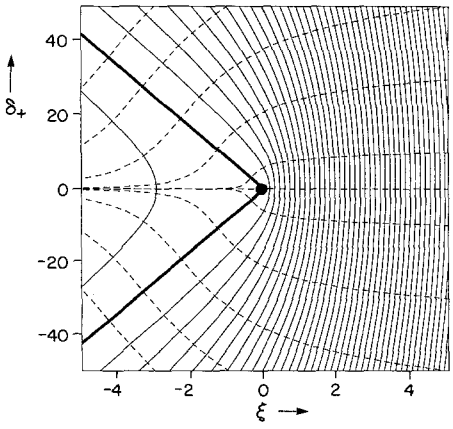

Fig. 6. Contours (*solid lines*) and orthogonal trajectories (*dashed lines*) of the surface $E - E(\mathrm{CR})$ for $\eta = 0$ in the ξ–δ_+ plane (FORS1/ii calculation). The intersection point (CR) lies at the origin (*heavy dot*). *Heavy solid lines*: contour $E - E(\mathrm{CR}) = 0$. Increment of contours: 0.5 mhartree

point $\eta = \delta_+ = 0$ belongs to the ICS, since none of the ICS-spanning coordinates $\eta, \gamma_1'', \gamma_2'', \ldots, \gamma_6'', \gamma_1', \gamma_2', \ldots, \gamma_6''$ are displayed. Along the bold contour for $\xi < 0$, the displayed energy E of the lower surface remains constant and equal $E(\mathrm{CR})$, whereas the upper state energy varies according to $E' - E(\mathrm{CR}) = -2 \times 1918\xi = 3836|\xi|$ michrohartree.

The preceding discussion shows that, at the intersection point CR, one steepest descent line arrives from $\xi < 0$ and one steepest descent line departs towards $\xi > 0$. The former originates at the transition state TS and first follows a valley which turns into a ridge at the inflection point I. The latter follows the ridge to the transition state TS*. The former is a reaction path model from TS to I but, thereafter, it corresponds to an unstable dynamic trajectory so that the system will be deflected from the ridge. Figure 6 shows, however, that all steepest descent lines close to the ridge swerve away from the ridge upon approaching the intersection point CR. This implies that the forces near CR have strong *bifurcating effect*. Thus, it seems reasonable to consider the region between I and CR as the bifurcating region. This conclusion was confirmed by starting a steepest descent line in the neighborhood of TS at the beginning of the thin line on Fig. 3. It followed the valley from TS to I, as indicated on the figure, and then effectively merged with the steepest descent line, discussed at the end of Sect. 4.2, which was obtained by starting near CR off the ridge, viz., at the point corresponding to $\xi = 0°$, $\delta_+ = 1°$ on Fig. 6.

An in-depth study of contours and steepest descent lines in the neighborhood of an intersection point will be presented in a separate publication [16].

5.5. Intersection coordinate subspace and reduced energy surfaces

In the discussion of the global features of the potential energy surface, in the first paper as well as in the discussion of the ring-opening transition state in Sect. 3.1 of the present paper, we relied heavily on the *reduced* potential energy surface which is easier to visualize. It is obtained by optimizing the energy for each choice of $(\Phi, \delta_1, \delta_2)$ and hence a function $E(\Phi, \delta_1, \delta_2)$. This function is the collection of all those points on the full surface $E(\phi, \delta_1, \delta_2, \gamma_1, \gamma_2, \ldots, \gamma_{12})$ which satisfy the twelve conditions:

$$(\partial E/\partial \gamma_j)_{\phi,\delta_1,\delta_2} = 0, \quad j = 1, 2, \ldots, 12 \tag{5.19}$$

In the present section we examine the relation between the reduced surface, and the intersection coordinate space. We must now deal with *two* reduced surfaces, namely:

$$E_1(\phi, \delta_1, \delta_2) \text{ defined by } (\partial E_1/\partial j_j)_{\phi,\delta_1,\delta_2} = 0, \quad j = 1, 2, \ldots, 12 \tag{5.20}$$

$$E_2(\phi, \delta_1, \delta_2) \text{ defined by } (\partial E_2/\partial j_j)_{\phi,\delta_1,\delta_2} = 0, \quad j = 1, 2, \ldots, 12 \tag{5.21}$$

Complications arise from the fact, for a given choice of $(\phi, \delta_1, \delta_2)$, the values of the optimized secondary coordinates $(\gamma_1, \gamma_2, \ldots, \gamma_{12})$ of $E_1(\phi, \delta_1, \delta_2)$ are in general different from those of $E_2(\phi, \delta_1, \delta_2)$.

Consider the 13-dimensional ICC in C_1. The twelve additional derivative conditions of Eq. (5.20) define a *line* on the ICS which is also a line on the reduced surface $E_1(\phi, \delta_1, \delta_2)$. Similarly, addition of the twelve derivative conditions of Eq. (5.21) will define another line on the ICS which, at the same time, lies on the reduced surface $E_2(\phi, \delta_1, \delta_2)$. In general, *these two lines on the ICS are not identical, they will not even intersect.*

Similar reasoning holds in the C_s-preserving subspace defined by $\delta_+ = \gamma_1' = \gamma_2' = \cdots = \gamma_6' = 0$. Since the derivatives with respect to these antisymmetric coordinates vanish automatically when C_s is preserved, the twelve Eqs. (5.19) can be replaced by the six conditions:

$$(\partial E/\partial \gamma_j'')_{\phi,\delta_-,\delta_+=0} = 0, \quad j = 1, 2, \ldots, 6 \tag{5.22}$$

These six additional conditions define a *line* in the 7-dimensional ICS in C_s which also lies on the reduced surface $E(\phi, \delta_+ = 0, \delta)$. Again, the lines corresponding to E_1 and E_2 are different and cannot be expected to intersect.

We believe that, for both reduced surfaces $E_1(\phi, \delta_1, \delta_2)$, $E_2(\phi, \delta_1, \delta_2)$ the ICS line found in C_1 symmetry is identical with that found for C_s symmetry, i.e., it lies entirely in the C_s-preserving subspace.

To illustrate these observations, we made calculations involving a further reduction of the potential energy surface by minimizing also with respect to δ_-. The resulting surfaces $E_1(\phi, \delta_+)$ and $E_2(\phi, \delta_+)$ were considered in the C_s-preserving subspace, i.e., for $\delta_+ = 0$. Thus, we examined the reduced energy curves $E_1(\phi)$, $E_2(\phi)$ which we obtained by setting $\delta_+ = 0$ and adding the respective conditions:

$$(\partial E_n/\partial \delta_-)_{\phi,\delta_+=0} = 0 \quad \text{with } n = 1, 2 \tag{5.23}$$

to Eq. (5.22). The two *solid* lines in Fig. 7, labeled A′ and A″, display the reduced energy curves for Φ ranging from 84° to 102°. The apparent intersection

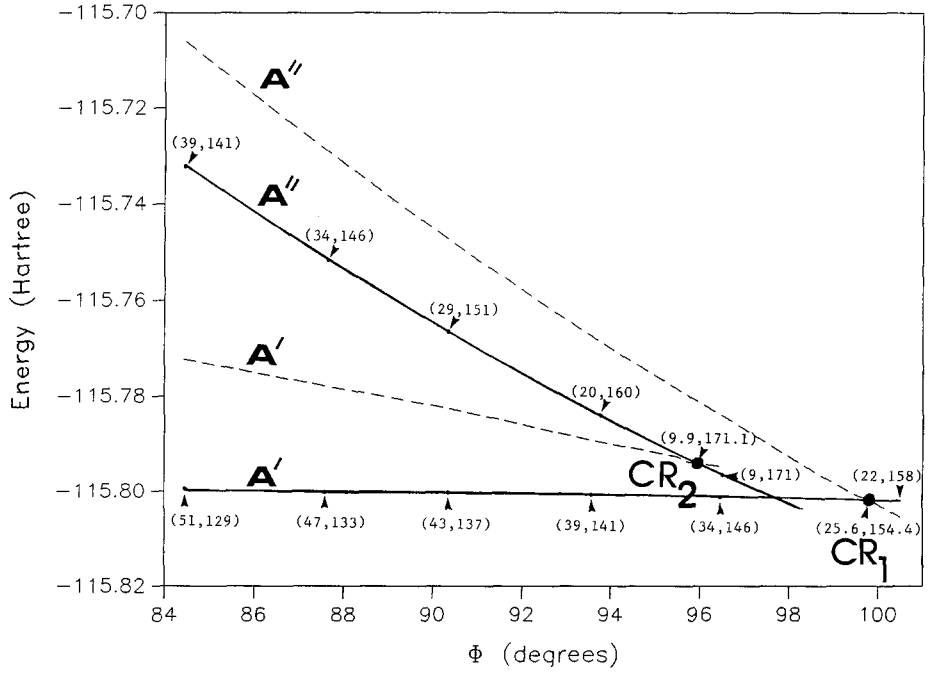

Fig. 7. Energies as functions of Φ for the $^1A'$, $^1A''$ surfaces in C_s near CR. See text for an explanation of the four curves. CR_1, CR_2: points on the intersection surface (*heavy dots*). Optimized values of (δ_1, δ_2) are shown in parentheses

of these two curves is not a true intersection since the two curves differ in the values of the optimized coordinates, in particular δ_-.

The intersection points CR_1 and CR_2 of the two curves with the ICS were determined as follows. For the optimized coordinates $(\delta_-, \gamma_1'', \ldots, \gamma_6'')$ of the A′ state (solid A′ line) we calculated the A″ energies at various ϕ values. The latter are plotted as the dashed line labeled A″ in Fig. 7 (which lies, of course, above the solid A″ line). The crossing point CR_1 of the solid A′ line and the dashed A″ line, is the point which the reduced surface $E_1(\phi)$ has in common with the ICS. Similarly, the dashed line labeled A′ (which lies above the solid A′ line) is a plot of A′ energies calculated for the coordinates $(\delta_-, \gamma_1'', \ldots, \gamma_6'')$ optimized for A″ (solid A″ line). The crossing point CR_2 of the dashed A′ and the solid A″ line is the point which the reduced surface $E_2(\phi)$ has in common with the ICS. The coordinates and energies for the various points on all these curves are listed in Table 8.

It can be seen that the two points CR_1 and CR_2 are fairly close to the earlier found point CR which lies on the steepest descent curve. All these points have C_s symmetry and lie on the ICS. One would therefore expect that the coordinates of CR, CR_1, CR_2 would satisfy Eqs. (5.8) which defines the ICS to first order near CR. From Tables 7 and 8 and Eq. (5.17) one finds the ξ-values $\xi(CR_1) = -0.23°$, $\xi(CR_2) = -1.73°$ which are indeed small.

6. The free internal rotation of the CH_2 groups

In paper I, we had found a very distinctive feature which dominated the potential energy surface, for Φ larger than about 100°, *outside* the C_s-preserving subspace, i.e., for $\delta_1 + \delta_2 \neq n \cdot 180°$ (n = integer). This was an almost free, cogwheel-like, synchronized internal rotation of the two CH_2 groups for fixed ring-opening angles. It was depicted by isoenergetic shelves in valleys which, approximately, followed the lines $\delta_1 + \delta_2 = 90° + n \cdot 180°$ (n = integer) on the contour panels Φ = constant > 100°. The panel for $\Phi = 100°$ is again displayed in Fig. 8a. The valley is seen to sway back and forth slightly from the line $\delta_1 + \delta_2 = 90°$ and it contains slight minima, the one denoted by m lying at $\delta_1 + \delta_2 = 37°$.

Since this is a very characteristic feature, it was considered important to confirm that it would be preserved by the more accurate calculations. To this end, we recalculated the entire panel for $\Phi = 100°$ at the (FORS1/ii) level and the resulting contours are displayed in Fig. 8b. While the absolute energies are, of course, different from those in paper I, the contour increment is the same as in Fig. 8a (5 mhartree). It is seen that the overall topography is the same in both figures, namely valleys weaving around the average line $\delta_1 + \delta_2 = (90° + n \cdot 180°)$ and separated by ridges following the lines $\delta_1 + \delta_2 = n \cdot 180°$. For the more accurate calculations, the maxima are somewhat broader and force a more undulatory character on the valleys. The valley minimum denoted by m occurs for $\delta_1 = \delta_2 = 29°$. However, the very slight barrier along the valley floor is almost the same for both calculations (2.5 kcal/mol for the calculations of paper I, 3.1 kcal/mol for the present calculation) and so is the energy difference between the minimum m and the maximum M (about 45 kcal/mol for both calculations).

There exists a slight possibility that the differences between the contours in Fig. 8a,b are somewhat exaggerated due to the method of calculation. In paper I, the contours of each panel were based on 50 points (see Sect. 2.3 of paper I).

Table 8. Internal coordinates corresponding to the points of Fig. 7

Geometries optimized in the $^1A'$ state									
Φ	84.45	87.50	90.47	93.50	96.50	99.70	99.80	99.90	100.50
δ_1	51.00	47.34	43.43	38.68	33.52	25.54	25.5819	25.20	23.10
δ_2	129.00	132.66	136.57	141.32	146.48	154.46	154.40813	154.80	156.90
r_{01}	1.422	1.418	1.417	1.416	1.416	1.417	1.417	1.416	1.417
r_{02}	1.422	1.418	1.417	1.416	1.416	1.417	1.417	1.416	1.417
r_{11}	1.079	1.080	1.080	1.081	1.082	1.083	1.083	1.084	1.084
$r_{11'}$	1.077	1.079	1.080	1.080	1.080	1.080	1.080	1.080	1.080
r_{22}	1.079	1.080	1.080	1.081	1.082	1.083	1.083	1.084	1.084
$r_{22'}$	1.077	1.079	1.080	1.080	1.080	1.080	1.080	1.080	1.080
α_{011}	117.8	118.1	118.5	119.0	119.6	120.2	120.2	120.2	120.3
$\alpha_{011'}$	127.2	126.9	126.6	126.1	125.7	125.2	125.1	125.2	125.0
α_{022}	117.8	118.1	118.5	119.0	119.6	120.2	120.2	120.2	120.3
$\alpha_{022'}$	127.2	126.9	126.6	126.1	125.7	125.2	125.1	125.2	125.0
β_1	1.3	0.75	2.4	3.3	3.7	3.0	3.1	3.2	3.0
β_2	1.3	0.75	2.4	3.3	3.7	3.0	3.1	3.2	3.0
$E(^1A')^a$	−.7995521	−.8001908	−.8003894	−.8007223	−.8011767	−.8018101	−.8018316	−.8018554	−.8019945
$E(^1A'')^a$	−.7059920	−.7281416	−.7480590	−.7670972	−.7841750	−.8014784	−.8018316	−.8022671	−.8054884
ΔE^b	93560.1	72049.2	52330.5	33625.1	17001.7	331.7	0.0	−411.7	−3493.9

Geometries optimized in the $^1A''$ state

Φ	84.43	87.50	90.50	93.50	94.50	95.60	95.80	95.90	96.50
δ_1	38.76	33.78	28.63	20.08	17.43	11.40	10.00	9.81	9.57
δ_2	141.24	146.22	151.37	159.92	162.57	168.60	170.00	171.19	170.43
r_{01}	1.488	1.473	1.460	1.449	1.446	1.442	1.441	1.441	1.439
r_{02}	1.488	1.473	1.460	1.449	1.446	1.442	1.441	1.441	1.439
r_{11}	1.087	1.085	1.084	1.082	1.082	1.081	1.081	1.081	1.081
$r_{11'}$	1.066	1.066	1.065	1.065	1.065	1.064	1.064	1.064	1.065
r_{22}	1.087	1.085	1.084	1.081	1.082	1.081	1.081	1.081	1.081
$r_{22'}$	1.066	1.066	1.065	1.065	1.065	1.064	1.064	1.064	1.065
α_{011}	120.6	121.1	121.3	121.9	121.8	122.2	122.2	122.2	121.9
$\alpha_{011'}$	121.0	121.4	121.8	123.3	122.4	122.5	122.6	122.6	122.7
α_{022}	120.6	121.1	121.3	121.9	121.8	122.2	122.2	122.2	121.9
$\alpha_{022'}$	121.0	121.4	121.8	123.3	122.4	122.5	122.6	122.6	122.7
β_1	23.1	20.1	17.2	12.0	10.6	6.9	6.0	5.9	6.0
β_2	23.1	20.1	17.1	12.0	10.6	6.9	6.0	5.9	6.0
$E(^1A')^a$	−.7722351	−.7776948	−.7828373	−.7891197	−.790722	−7934577	−.7937621	−.7938668	−.7947898
$E(^1A'')^a$	−.7319736	−.7506926	−.7674067	−.7826448	−.7874235	−.7925057	−.7934165	−.7938668	−.7965220
ΔE^b	40261.5	27002.2	15430.6	6474.9	3448.7	952.0	345.7	0.0	−1732.2

[a] $E + 115.0$ hartree

[b] $E(^1A'') - E(^1A')$ in microhartree

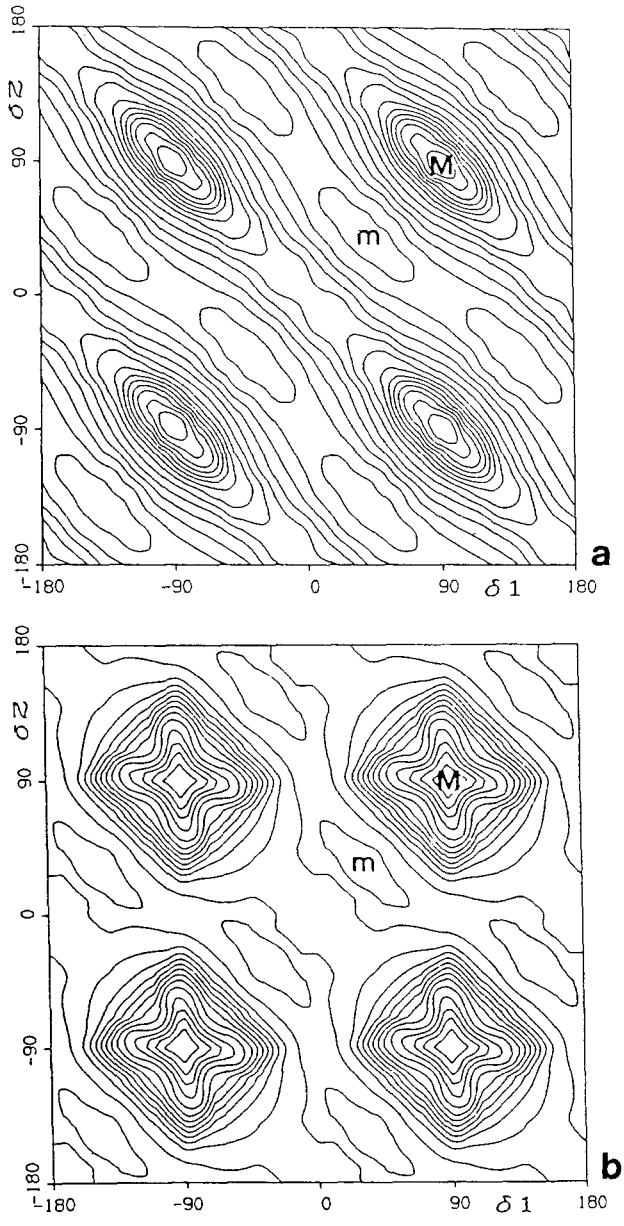

Fig. 8a,b. Contour plots of the reduced energy surface $E(\Phi, \delta_1, \delta_2)$ for $\Phi = 100$: **a** FORS1/i calculation; **b** FORS1/ii calculation. Contour increment: 5 mhartree in both cases. *m*: minimum *M*: maximum

We found, however, that the contour map for $\Phi = 100°$ in paper I remained virtually unchanged when only the 25 points:

$$\delta = 20n_1 + 10n_2 \qquad \delta_2 = 10n_2$$

$$n_1 = 0, 2, 4, \ldots, (9 - n_2) \qquad n_2 = 1, 3, 5, 7, 9$$

were used. Therefore, the more accurate calculations were only performed at

these points and the contours of both, Fig. 8a,b, are based on this set of points. It is possible, although not too likely, that the two contour maps might look more similar to each other, had both been based on 50 points.

Incidentally, the savings in computing time hoped for by calculating only 25 points were not realized because the reduction in the number of points was offset by the increase in computation needed for each point $(\Phi, \delta_1, \delta_2)$. This was so since, due to the larger distance between the individual 25 points, the initial approximations to the geometries of the 12 secondary coordinates were poorer as were the starting orbitals for the MCSCF calculations. Consequently, convergence was considerably slower for both these iterative procedures.

7. Conclusions

In the present sequence of investigations, insight in the cyclopropylidene-allene ring opening has been gained on the basis of the potential energy surface governing this reaction. The global overall features of the surface were established in the first paper and the specific topographies of its key regions were determined in the present paper. In the second paper, the changes in molecular geometry along the reaction paths and the critical energy differences were related to the electronic rearrangements through a bonding analysis in terms of intrinsic quasiatomic molecular orbitals.

In order to be able to deal with an energy surface of such an extent, the appropriate formulation and separation of primary and secondary internal coordinates were essential. The former describe the ring opening and the rotations of the two CH_2 groups and were treated as independent variables. The latter describe the remaining degrees of freedom and were relaxed for the various choices of the former. The discussion was then based on the *reduced* energy surface, i.e., the energy as a function of the three independent primary coordinates. This surface exhibits a variety of nontrivial features requiring specific analyses. The reaction path quickly ascends from the reactant minimum to the transition state which lies on an extremely flat plateau. Shortly thereafter, between a valley-ridge inflection point an a conical intersection both of which are located on the steepest descent line coming from the transition state, the reaction path bifurcates. After that, upon the descent to the products, it becomes non-unique because it crosses slopes of long isoenergetic valleys corresponding to free internal motions.

The intersection point presents a certain conceptual difficulty because it is not possible to define a "reduced" (in the sense defined above) intersection space. (In the first paper where the global shape of the energy surface was established, the region around the intersection point was not explored in detail and the global contour plots given there gloss over the local features of this region. Also, in the minimal-basis-set approximation used in that paper, the reaction path bypasses the intersection because it bifurcates before the transition state.)

The chemical inferences are as follows. The reactant cyclopropylidene is a bona fide molecule with a singlet ground state which should be stable at low enough temperatures. It has C_{2v} symmetry with the two CH_2 groups standing perpendicular to the plane of the almost equilateral triangle of the three carbon atoms. During the initial stage of the ring opening, the CH_2 groups rotate towards each other in a disrotatory fashion maintaining C_s symmetry. This symmetry is also preserved at the transition state which occurs for a ring-opening

angle of about 84.5° with a barrier of about 7 kcal/mol. The C_s-preserving disrotatory motion continues for the further opening of the ring from 85° to about 100° and, during this phase of the internal motion, the energy decreases only by about 2 kcal/mol.

At about 100°, the ground-state surface intersects the lowest singlet excited state and, near this intersection, the two CH_2 groups switch to a conrotatory motion, one of them rotating further towards the CCC plane, the other away from it, so that C_s symmetry is broken. There are two alternative options, depending on which CH_2 group rotates in which direction, resulting in two bifurcating reaction paths which are each other's mirror images and lead to the two allene isomers which are each other's chiral isomers (assuming the numbered hydrogen atoms can be distinguished). The energy decreases rapidly during this stage of the reaction. The product allene lies 65 kcal/mol below the reactant. Both bifurcating pathways are equally likely and any stereospecificity of the reaction involving the deuterium-substituted system would be entirely due to the dynamic effect of the mass difference. This result also suggests that the stereospecificity observed in other substituted species is most likely due to non-covalent steric and long-range electrostatic effects, a conjecture which will be examined in the subsequent paper.

On the energetically downhill pathways after the bifurcation, the molecule furthermore finds itself in a state where the two CH_2 groups can rotate freely in a synchronized cogwheel-like fashion. Any stage of this disrotatory motion leads to the staggered allene product because the synchronized motion of the two CH_2 groups degenerates into a rigid-body rotation of the allene molecule around its CCC axis when the ring-opening angle becomes 180°.

It must also be recognized that there is a definite probability for the molecule to pass *diabatically* into the excited singlet state which it crosses at a ring-opening angle of about 100°. When this happens, the product will be the equilibrium structure of the excited state at an opening angle of 106° which is a planar structure. This excited surface was not studied in further detail.

A reaction path also exists for the isomerization from one allene isomer to the other. Its transition state is a planar structure with a ring-opening angle of 135° so that the molecule will bend about 45° when it isomerizes. The barrier is about 45 kcal/mol.

The described features of the reaction can be understood in terms of changes in orbital occupations and orbital energies. The reactant cyclopropylidene has carbene character with essentially a sigma lone pair at the center atom and a sigma bond between the end atoms. The product allene has a σ-bond and a π-bond between the center atom and each of the end atoms. At the intermediate geometries, including both transition states, the system has a delocalized pi-system covering all three atoms. Details are discussed in the preceding paper [14].

We believe that the described richness of features is not peculiar to the surface considered here. Rather, this is the first *extensive ab initio* exploration of a surface involving more than three atoms. A similar variety of features may be common among potential energy surfaces governing chemical reactions between polyatomic molecules.

References

1. Valtazanos P, Elbert ST, Ruedenberg K (1991) Theor Chim Acta 78:287 (Paper 1)
2. Dykstra CE, Schaefer HF III (1980) in: Patai S (ed) The chemistry of ketenes, aldehydes and related compounds, Wiley Interscience, New York, p 1, and references therein

3. Ruedenberg K, Sundberg KR (1976) in: Galais JL, Linderberg J, Goscinski O, Ohrn Y (eds) Quantum science, structure and method, Plenum Press, New York
4. Dunning TH, Hay PJ (1971) in: Schaefer HF (ed) Methods of electronic structure theory, Plenum Press, New York, p 1
5. See Ref. [4]
6. Schmidt MW, Ruedenberg K (1979) J Chem Phys 71:3951
7. Raffenetti RC (1973) J Chem Phys 58:4452; Feller DF, Ruedenberg K (1979) Theor Chim Acta 52:231
8. Dupuis M, Spangler D, Wendoloski JJ (1980) Nat Resour Comput Chem Software Cat 1, Prog. No. QGO1 (GAMESS)
9. Elbert ST, Cheung LM, Ruedenberg K (1980) Nat Resour Comput Chem Software Cat 1, Prog. No. QMO1 (ALIS)
10. Edmiston C, Ruedenberg K (1963) Rev Mod Phys 35:457; England W, Salmon LS, Ruedenberg K (1971) Topics in Current Chemistry 23:31, and references therein
11. Ruedenberg, Valtazanos P (1986) Theor Chim Acta 69:281
12. Herzberg G (1966) in: Molecular spectra and molecular structure III. Electronic spectra of polyatomic molecules, Van Nostrand Reinhold, New York, p 640
13. Warner P (private communication)
14. Xantheas S, Valtazanos P, Ruedenberg K (1991) Theor Chim Acta 78:327 (Paper 2)
15. Teller E (1937) J Phys Chem 41:109
16. Atchity G, Xantheas S, Ruedenberg K (to be published)